The Electrochemical Society
Advancing solid state & electrochemical science & technology

Production of Iron Alloy by Direct Electrolytic Reduction Using Suspension Electrolysis in an Alkaline Electrolyte

View the article online for updates and enhancements.

Production of Iron Alloy by Direct Electrolytic Reduction Using Suspension Electrolysis in an Alkaline Electrolyte

Manabu Tokushige,[1,z] Ole Edvard Kongstein,[2] and Geir Martin Haarberg[1,*]

[1]*Department of Materials Science and Engineering, Norwegian University of Science and Technology, Trondheim NO-7491, Norway*
[2]*Department of Applied Mechanics and Corrosion, Division of Materials and Chemistry, SINTEF, Trondheim, NO-7465, Norway*

Iron alloys were produced by suspension electrolysis in a 50 *wt%* NaOH–H_2O electrolyte at 383 K, and Fe–Cr and Fe–Ni alloys were obtained using a suspension of Fe_2O_3+Cr_2O_3 and Fe_2O_3+$Ni(OH)_2$ particles, respectively. Highly ordered columnar deposits comprising cubic Fe–Cr particles with approximately 5-micrometer-long sides were obtained on a disk cathode with a current efficiency higher than 90% at 100–300 mA·cm^{-2}. In contrast, disordered columnar deposits of Fe–Ni particles with diameters of approximately 1.0 μm were obtained on a disk cathode with a current efficiency of approximately 50% at 200 mA·cm^{-2}. The proposed method affords iron alloys with compositions in the stainless-steel region that depend on the electrolysis conditions, namely, the current density and Fe_2O_3/Cr_2O_3 or Fe_2O_3/$Ni(OH)_2$ content ratio.

© 2022 The Electrochemical Society ("ECS"). Published on behalf of ECS by IOP Publishing Limited. [DOI: 10.1149/1945-7111/ac9b97]

Iron and iron alloys are essential to modern society as structural and functional materials. For example, stainless steel, which is produced by alloying iron with chromium and/or nickel to improve corrosion resistance (Cr: 4.0–18 *wt%* and Ni: 12–20 *wt%*) and hardness (Cr: 0.5–2.0 *wt%* and Ni: 2.0–5.0 *wt%*), is used in a variety of fields ranging from architecture and locomotion to medicine. Iron is conventionally manufactured by the carbothermic reduction of iron ore using coke in a blast furnace, which produces large amounts of carbon dioxide.

Recent demands for reducing greenhouse-gas emissions necessitate alternative methods for iron manufacture. Therefore, we investigated an electrochemical process for producing iron.[1–4] In this method, a suspension of solid oxide particles were electrolyzed and directly reduced in a strongly alkaline electrolyte to produce a metallic phase on the surface of a rotating-disk cathode (RDE).[1–9] This method can produce various kinds of metals without emitting CO_2, is easily scalable, and consumes energy at a rate of 2.4–26 W kg^{-1} of Fe (100–300 mA·cm^{-2}).[1] The method employs 50 *wt%* of NaOH–H_2O at 383 K, conditions that have been previously determined to be suitable for iron-oxide electrolysis.[10] Iron was obtained on a rotating-disk cathode by direct reduction of solid hematite (Fe_2O_3) particles with a current efficiency higher than 95% (100–300 mA·cm^{-2}).[1] Our previous study[1] confirmed that Fe_2O_3 particles receive electrons at the cathode surface and are reduced, while OH$^-$ ions dissolve in the electrolyte (reaction 1). Fe_3O_4 is adsorbed and directly reduced on the cathode surface by reaction 2:

$$3/2Fe_2O_3 + 1/2H_2O + e^- \rightarrow Fe_3O_4(FeO + Fe_2O_3) + OH^- \quad [1]$$

$$FeO + H_2O + 2e^- \rightarrow Fe + 2OH^- \quad [2]$$
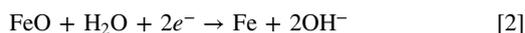
These processes are consistent with the E-*p*H diagram of Fe–H_2O (Fig. 1).[11] Furthermore, this method produces iron alloys from Fe_2O_3 and other coexisting oxide particles (e.g., Cr_2O_3, Fig. 2). Although the E-*p*H diagram of Cr–H_2O (Fig. 3a)[11] shows that significant energy is required for the electrodeposition of Cr in an alkaline electrolyte, the alloying process can lower the energy requirement. This is because the activity of Cr in the Fe–Cr alloy is lower than unity.[12,13] Electrochemical methods for producing iron alloys employ acidic aqueous electrolytes (*p*H = 0–3) with dissolved chlorides, sulfates, etc. as metallic ion sources.[14–37] Fuseya and

Sasaki[14] obtained Fe–Cr deposits with Cr compositions of 5.0–65 *at* % at 80–250 mA·cm^{-2}, with a current efficiency of less than 14% in a sulfate electrolyte. Wang and Watanabe[15,16] produced Fe–Cr deposits with Cr compositions of 3.1–74 *at%* at 50–250 mA·cm^{-2} from a chloride source, while Yagi et al.[17,18] fabricated a Fe–Cr layer on a Fe substrate with a current efficiency of approximately 21% using sulfate sources. Although trivalent chromium ions were used in these studies, highly toxic hexavalent ions were generated therein by proportionation/disproportionation reactions. Furthermore, an efficient production of Fe–Cr was difficult, owing to the low H_2-evolution overpotential of the acidic electrolyte.

Fe–Ni electrodeposition has been widely studied using chloride and/or sulfate electrolytes, and electrolyte contents, including the Fe^{2+}/Ni^{2+} concentration ratio and *p*H, suitable for a sustainable electrolysis have been particularly investigated, because they determine the Fe–Ni compositions and current efficiencies of the obtained deposits.[19–28] Su et al.[19] obtained Fe–Ni deposits with wide-ranging Ni compositions (3.8–85 *at%*) using dilute chloride sources ($NiCl_2$·$6H_2O$: 0.1–1.0 M) and confirmed that the current efficiency increased from 25% to 52% at 100–800 mA·cm^{-2}. However, chlorides and sulfates are usually prepared from oxides by chlorination and sulfation, respectively. Therefore, our method, which affords the electrodeposits directly from the oxide, is clearly advantageous.

Brenner classified Fe–Ni codeposition in an acidic electrolyte as "anomalous."[29] The electrochemical reduction of Ni^{2+} in the presence of Fe^{2+} is inhibited compared to its deposition from a pure Ni^{2+}-containing electrolyte. In contrast, the reduction of Fe^{2+} is faster in the presence of Ni^{2+}, owing to the formation and adsorption of hydroxides. During electrolysis, the interfacial *p*H in the vicinity of the cathode increases, owing to H_2 evolution and hydroxide production. Dahms and Croll[30,31] proposed that the preferential precipitation of $Fe(OH)_2$ over $Ni(OH)_2$ inhibits Ni deposition. To explain the anomalous codeposition observed under less-alkaline conditions, Hessami and Tobias[32] assumed hydroxide ions to be the primary deposition precursors, which competed with each other for surface sites, and attributed the anomalous codeposition to the hydroxide-concentration difference due to the dissociation constant. In this study, the use of solid reductant particles as iron sources eliminated these anomalies.

Herein, we investigated the feasibility of iron-alloy production using suspension electrolysis by examining the formation of Fe–Cr and Fe–Ni as model materials, using Cr_2O_3 and $Ni(OH)_2$ particles as the chromium and nickel sources, respectively. $Ni(OH)_2$ particles are scarcely soluble and were suspended in the NaOH–H_2O

*Electrochemical Society Member.
zE-mail: tokushige.manabu@gmail.com
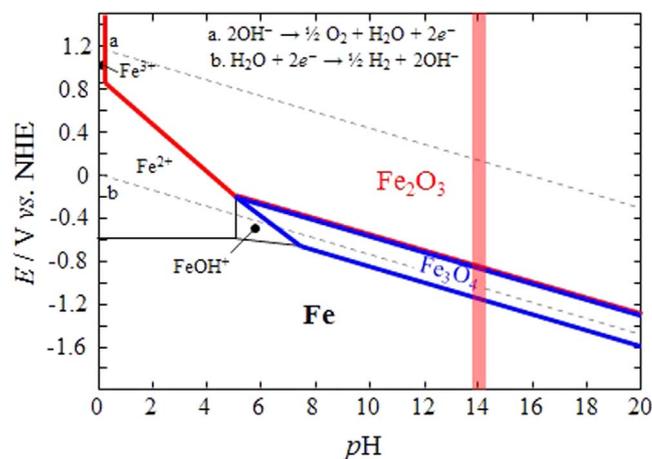
Figure 1. E-pH diagram of Fe–H_2O at 373 K.[11]
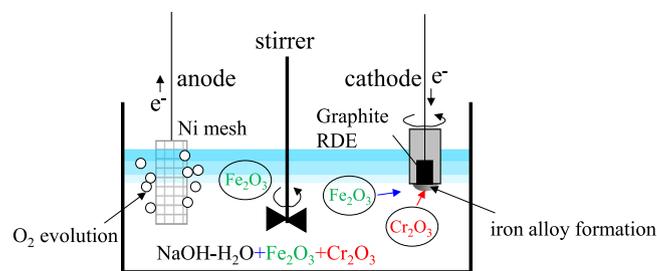
Figure 2. Principle for the production of iron alloys via direct reduction, using suspension electrolysis of oxide particles in NaOH–H_2O. Example: Production of Fe–Cr using suspended Fe_2O_3 and Cr_2O_3 particles.

electrolyte.[33] The relationships between the alloy compositions of the obtained deposits and the electrolysis conditions, namely the current density and Fe_2O_3/Cr_2O_3 or Fe_2O_3/Ni(OH)$_2$ content ratio, were evaluated.

Experimental

Figure 4 shows the experimental setups. Suspension electrolysis was conducted in 50 *wt%* NaOH–H_2O (NaOH: 99.0% purity, VWR International, LLC, USA) at 383 K. Fe_2O_3 (99.5% purity, 325 mesh, Alfa Aesar Gmbh & Co. KG, Germany) and Cr_2O_3 (98% purity, 325 mesh, Alfa Aesar) particles with diameters less than 200 nm (Figs. 5a and 5b) and Ni(OH)$_2$ particles (Sigma-Aldrich Co. LLC, USA) with diameters of approximately 5.0 μm (Fig. 5c) were suspended in the electrolyte by agitation using a stirrer (500 rpm). Electrochemical experiments were performed using an IM6 electrochemical workstation (Zahner Gmbh & Co. KG, Germany) with a three-electrode cell. A rotating graphite disk (ø8.0 mm; 1,000 rpm) was used as the working electrode (cathode), and a Ni mesh was used as the counter electrode (anode) during the preparation of Fe–Cr (Fig. 4a), while a graphite rod (ø8.0 mm) was used during Fe–Ni production (Fig. 4b). An Hg/HgO electrode was immersed in a 0.1 M NaOH–H_2O reference solution, which was connected to the electrolyte via a salt bridge, and used as the reference electrode. Potential values were calibrated against a dynamic hydrogen electrode (DHE), where hydrogen evolution began on a Pt-wire (ø1.0 mm) cathode.

The obtained deposits, which were first immersed in distilled water and then in ethanol to remove the electrolyte, were characterized by X-ray diffractometry (XRD; Bruker-AXS D5005, Siemens, Germany) and field-emission scanning electron microscopy (FE-SEM; SU-6600, Hitachi High-Technologies Corp., Japan). The alloy compositions of the deposits were analyzed by energy dispersive

(a)

(b)
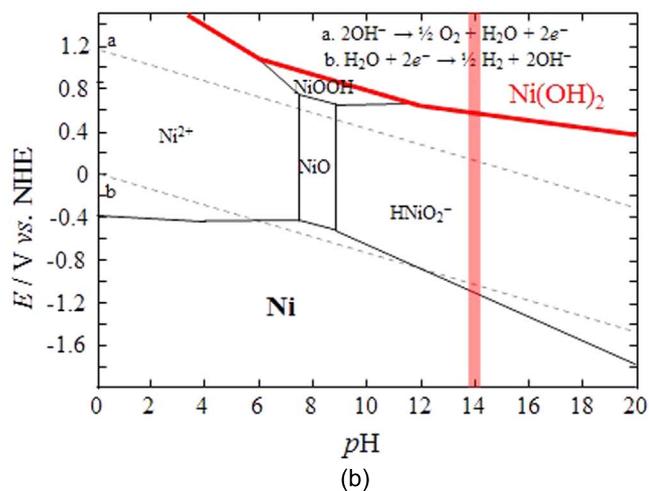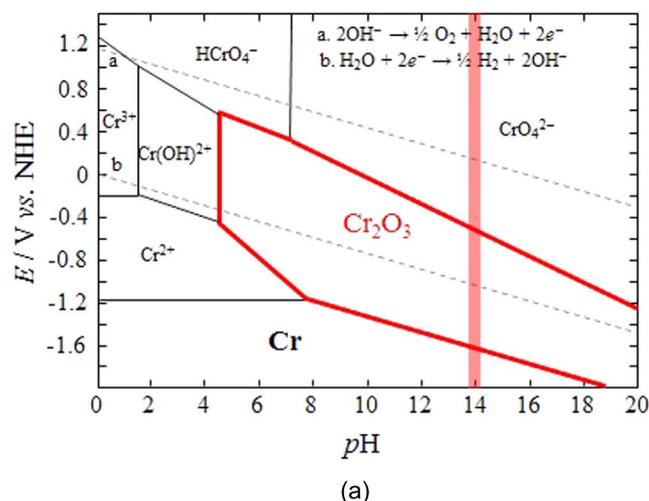
Figure 3. E-pH diagrams of Cr–H_2O (a) and Ni–H_2O (b) at 373 K.[11]

X-ray spectroscopy (EDS; XFlash 5010, Bruker Nano GmbH Berlin, Germany).

Results and Discussion

Fe–Cr production.—Figures 6a and 6b show the EDS spectrum and SEM images, respectively, of the deposit obtained on the cathode disk after electrolysis (100 mA·cm^{-2}, 6 h) in 50 *wt%* of NaOH–H_2O using suspended Fe_2O_3 particles (33 *wt%*) and Cr_2O_3 particles (5.0 *wt%*) at 383 K; EDS revealed that this deposit was $Fe_{86}Cr_{14}$ (Table I). The SEM images reveal columns approximately 50 and 300 μm in diameter and length, respectively, constructed from cubic particles with approximately 5-micrometer-long sides, while the XRD patterns (Fig. 7) show that the deposits were composed only of *bcc* Fe–Cr solid solutions. We confirmed that Fe_2O_3 and Cr_2O_3 particles were directly reduced on the cathode surface to form high-aspect Fe–Cr columns. The Cr ratio in the Fe–Cr deposit was higher at a higher current density (Fig. 8). Because the Fe–Cr deposits mainly consisted of Fe, we concluded that Fe_2O_3 particles were primarily reduced with Fe particles growing on the cathode during electrolysis and Cr_2O_3 particles reduced on the Fe phase directly to form Fe–Cr. Steady-state polarization curves in 50 *wt%* NaOH–H_2O electrolyte (Fig. 9) revealed that polarization increased upon addition of Cr_2O_3 particles to the electrolyte in which the Fe_2O_3 particles had been suspended, indicating a higher reduction energy of Cr_2O_3 than Fe_2O_3. This is consistent with thermodynamic calculations; the Gibbs energy changes for the reductions of Cr_2O_3 and Fe_2O_3 at 400 K were
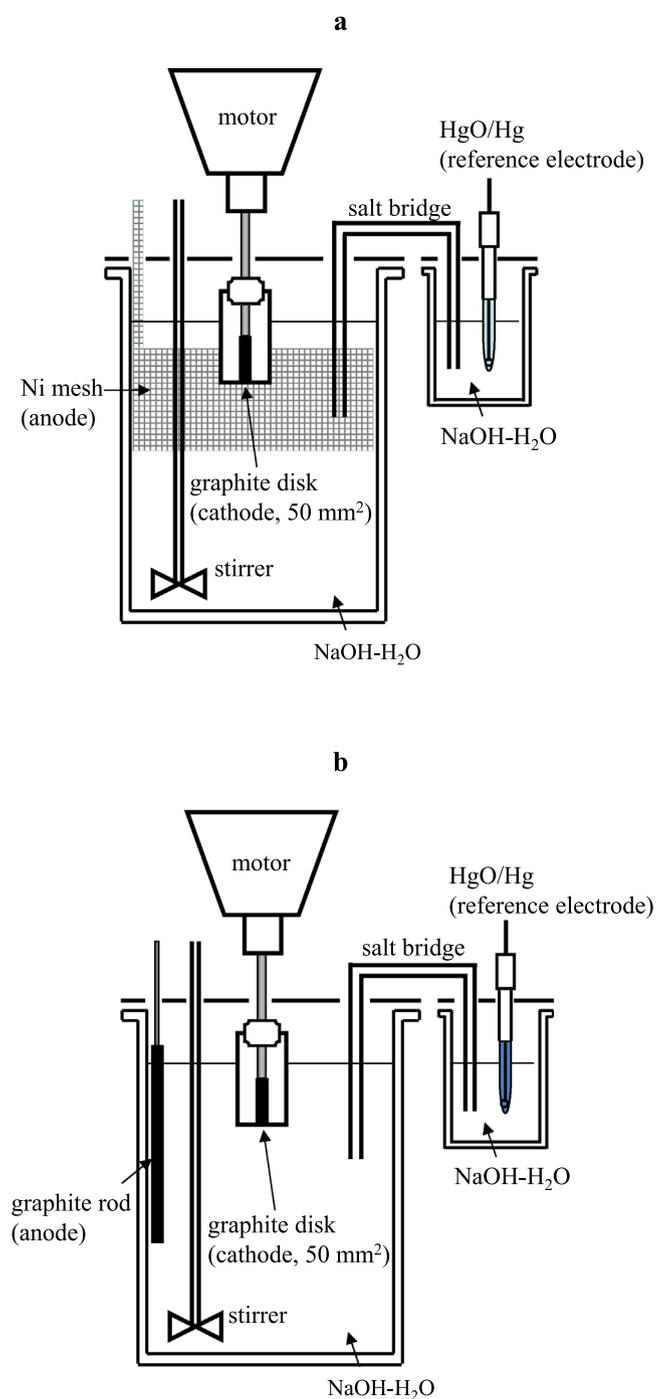
Figure 4. Experimental setups for the production of Fe–Cr (a) and Fe–Ni (b).

Figure 5. SEM images of Fe_2O_3 (a), Cr_2O_3 (b), and $Ni(OH)_2$ (c) particles.

353 and 43.0 kJ·mol^{-1}, respectively.[34] In contrast, polarization decreased with increasing Cr_2O_3-particle content, owing to the larger contribution of Cr_2O_3-particle reduction to the cathodic current. This indicates that the formation energy of Fe–Cr was lower than that for the reduction of the Cr_2O_3 particles, which is ascribable to a lower Cr-deposition energy, owing to a decrease in the activity of Cr deposition associated with alloy formation. As for the influence of current density on morphology, the columns overlapped to form a compacted deposit with a smooth surface at 40 mA·cm^{-2} (Fig. 10a), owing to a slower perpendicular growth compared to nucleus transport, as a result of the low overpotential.

Highly ordered Fe–Cr columns were obtained at 100 and 200 mA·cm^{-2} (Figs. 6b and 10b); columns approximately 10 and 130 μm in diameter and length were obtained from cubic particles approximately 2.0 μm in size at 200 mA·cm^{-2}. The columns were spindled and randomly orientated, and the deposit surface was not compact when formed at 300 mA·cm^{-2} (Fig. 10c). The average cubic particle size involved in column formation was lower, and the

a

b
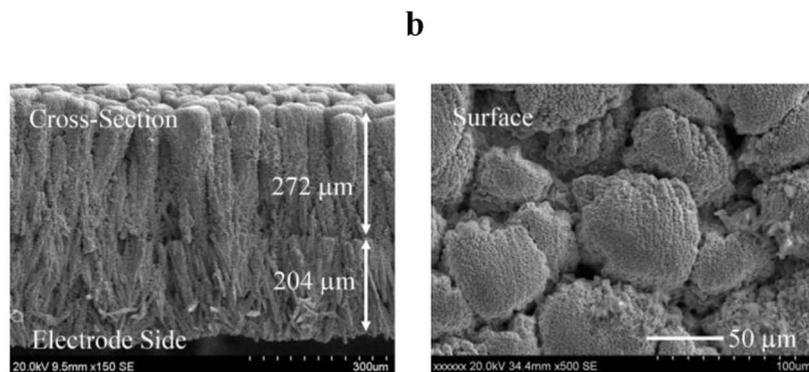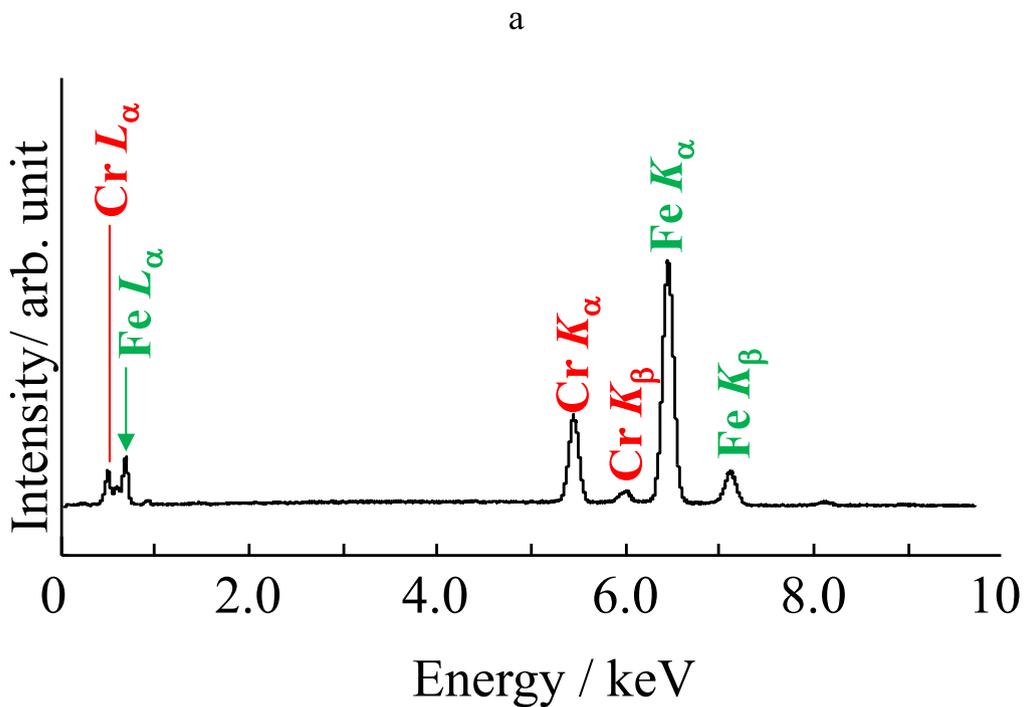
Figure 6. EDS spectrum (a) and SEM images (b) of the deposit obtained after electrolysis (100 mA·cm^{-2}, 6 h) in 50 *wt%* of NaOH–H$_2$O+Fe$_2$O$_3$ (33 *wt%*) + Cr$_2$O$_3$ (5.0 *wt%*) at 383 K.
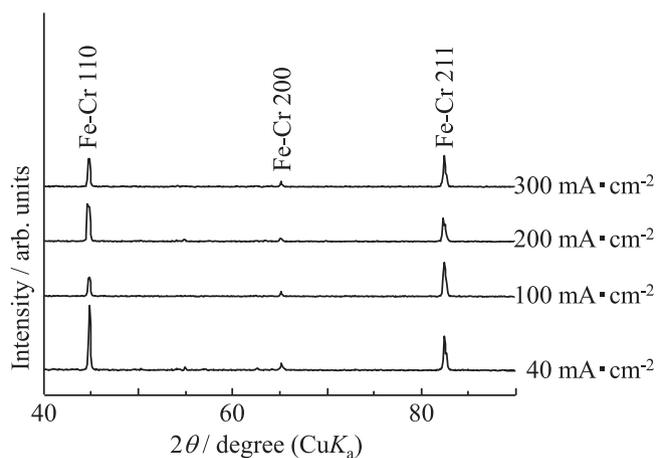
Figure 7. XRD patterns of Fe–Cr deposits obtained at various current densities via electrolysis in 50 *wt%* of NaOH–H$_2$O+Fe$_2$O$_3$ (33 *wt%*) + Cr$_2$O$_3$ (5.0 *wt%*) at 383 K Quantity of electricity: 1080C.
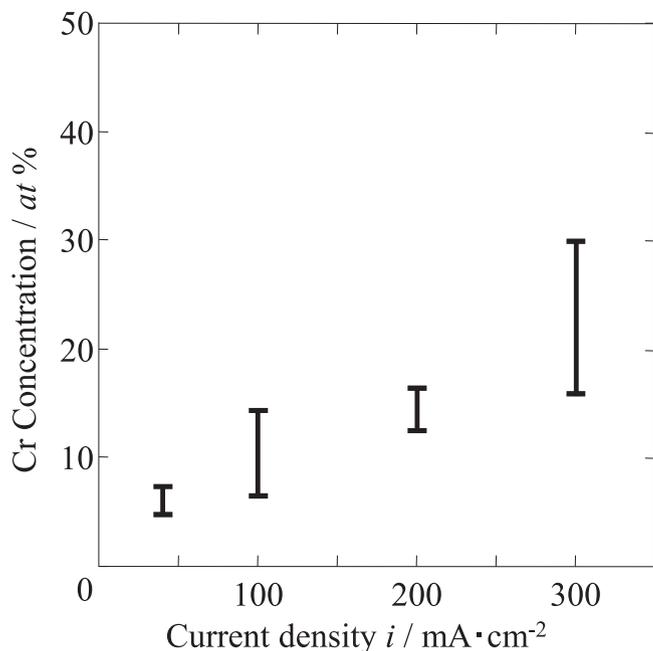
Figure 8. Fe–Cr composition as a function of current density in 50 *wt*% of NaOH–H_2O + Fe_2O_3 (33 *wt*%) + Cr_2O_3 (5.0 *wt*%) at 383 K. Quantity of electricity: 1080C.
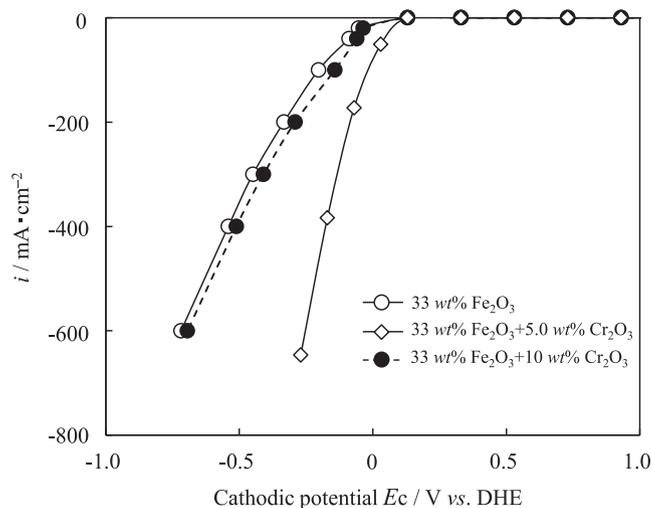
Figure 9. Typical steady-state polarization curves obtained in a 50 *wt*% NaOH–H_2O electrolyte at 383 K.

columns were spindled, at a higher overpotential. This tendency can be explained by the overpotential-dependence of the crystal growth rate; the columns become spindled by rapid perpendicular growth at higher overpotentials, and they are randomly orientated owing to weak support from the substrate.

In contrast, CrO powder was obtained after electrolysis by piling Cr_2O_3 powder on the cathode (Fig. 11). The observed diffraction pattern was ascribed to CrO with a cubic *Fm-3m* structure.[35] These results indicate that Cr_2O_3 was reduced in two steps:

$$1/2Cr_2O_3 + 1/2H_2O + 1/2e^- \rightarrow CrO + OH^- \qquad [3]$$

$$CrO + H_2O + 2e^- \rightarrow Cr(on\ Fe) + 2OH^- \qquad [4]$$
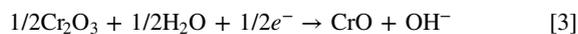
The adsorbed CrO was subsequently reduced to the Fe–Cr phase.

Table I. EDS-determined composition of the deposit obtained after electrolysis (100 mA·cm^{-2}, 6 h) in 50 *wt*% NaOH–H_2O + Fe_2O_3 (33 *wt*%) + Cr_2O_3 (5.0 *wt*%) at 383 K.

Element	*wt*%	*at*%
Fe	86.5	85.6
Cr	13.5	14.4

Table II. EDS-determined compositions of the Fe–Cr deposits obtained after electrolysis in 50 *wt*% of NaOH–H_2O + Fe_2O_3 (33 *wt*%) + Cr_2O_3 (10 *wt*%) at 383 K. Current density: (a) 100 mA·cm^{-2} and (b) 200 mA·cm^{-2} Quantity of electricity: 1080 C.

Element	*wt*%	*at*%
(a)		
Fe	86.1	85.2
Cr	13.9	14.8
(b)		
Fe	84.1	83.2
Cr	15.9	16.8

SEM images and EDS data for the Fe–Cr deposits, obtained using 10 *wt*% of the Cr_2O_3 particles, are shown in Fig. 12 and Table II, which reveal that Fe–Cr columns with higher Cr concentrations were obtained at higher Cr_2O_3 particle contents, confirming that the Fe–Cr composition can be controlled by the current density and Fe_2O_3/Cr_2O_3 content ratio. Figure 13 shows the dependences of the current efficiencies on the current densities, which were determined by applying Faraday's law to reactions 1–4, using the weights and compositions of the Fe–Cr deposits. The current efficiency increased from 51% to 96% as the current density increased from 40 to 100 mA·cm^{-2}, and it exceeded 95% at current densities of 100–200 mA·cm^{-2}. However, a lower current efficiency was observed at 300 mA·cm^{-2}. A similar dependence was observed during the formation of Fe from hematite.[1,2] These results can be explained in terms of the overpotential; the oxides were not smoothly reduced at 40 mA·cm^{-2}, owing to a low overpotential, and some electricity was consumed for H_2 evolution. A decent current-efficiency trend was observed above 300 mA·cm^{-2}; sparse columnar deposits were formed via rapid crystal growth, owing to a high overpotential, with some columns falling away from the deposit.

Fe–Ni production.—The method developed in this study produces a metal or alloy by the direct reduction of insoluble metallic ore particles suspended in an electrolyte. Despite focusing on oxides and examining the direct reduction of NiO particles, neither Ni nor its alloy could be obtained at a medium temperature of 383 K. Therefore, we focused on $Ni(OH)_2$ particles as an alternative nickel source for the iron-alloy formation, using hematite ore particles in an NaOH–H_2O electrolyte. $Ni(OH)_2$ particles are scarcely soluble and were suspended in the electrolyte.[33] Cyclic voltammograms were obtained using a rotating-graphite-disk electrode (1000 rpm) at various $Ni(OH)_2$-particle contents (Fig. 14). A redox current appeared at 0.2 V when $Ni(OH)_2$ particles were added, and it increased with the $Ni(OH)_2$ content, suggesting its association with the electrochemistry of the $Ni(OH)_2$ particles (reaction 5). The anodic current peak was smaller than that of the cathodic current during the anodic sweep, indicating that the Ni deposited on this electrolyte was in a passive state. In contrast, an anodic current peak was observed at 1.8 V corresponding to the oxidation of $Ni(OH)_2$ particles (reaction 6):[36]
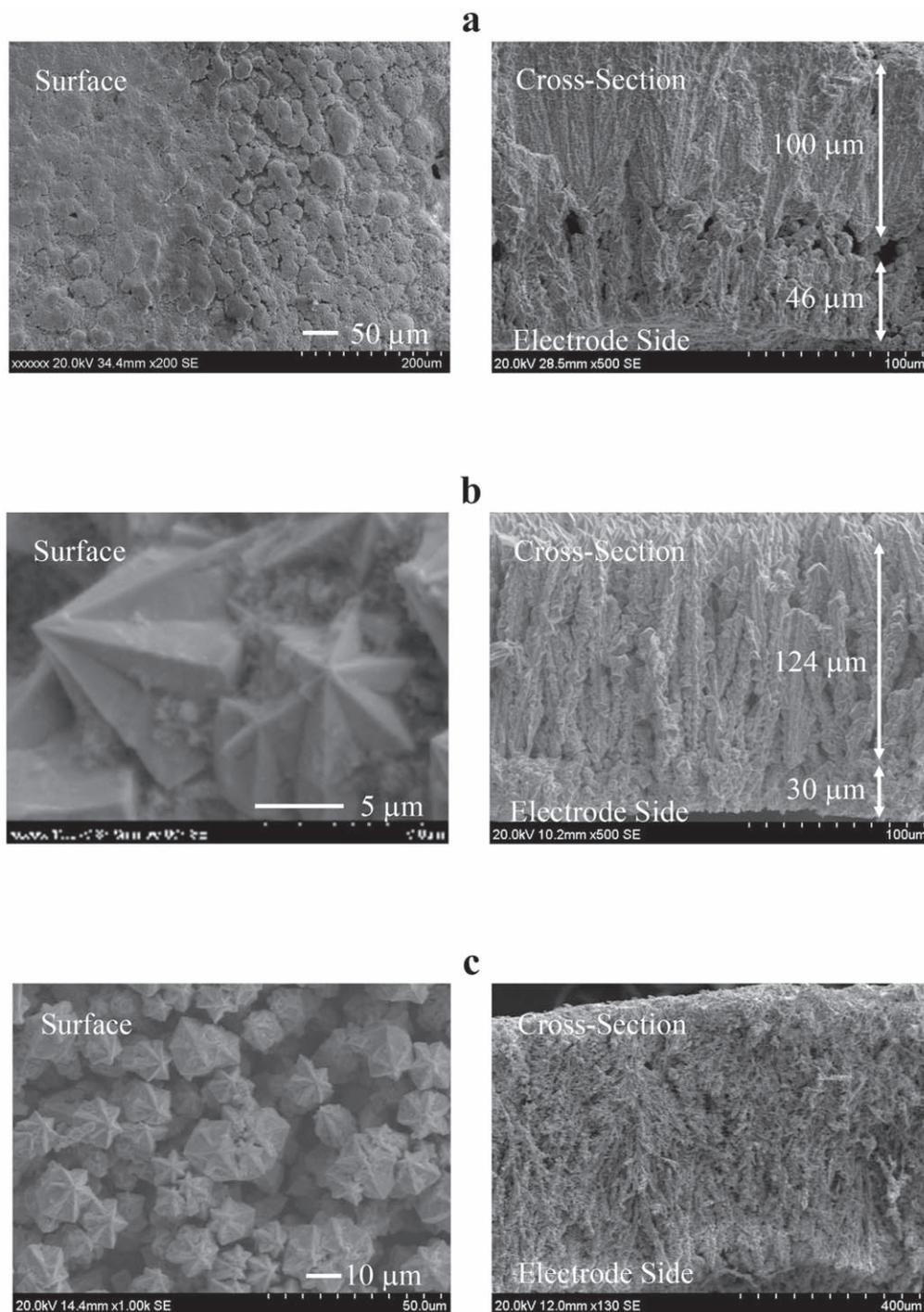
Figure 10. SEM images of Fe–Cr deposits obtained after electrolysis in 50 *wt%* of NaOH–H$_2$O + Fe$_2$O$_3$ (33 *wt%*) + Cr$_2$O$_3$ (5.0 *wt%*) at 383 K. Current density: 40 (a), 200 (b), and 300 (c) mA·cm^{-2} Quantity of electricity: 1080C.

$$Ni(OH)_2 + 2e^- \rightleftarrows Ni + 2OH^- \qquad [5]$$

$$Ni(OH)_2 + OH^- \rightleftarrows NiOOH + H_2O + e^- \qquad [6]$$
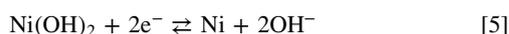
Figure 15 shows the XRD patterns and SEM images of the deposit obtained on the cathode after the electrolysis (1.0 A·cm^{-2}, 12 h) using 6.0 *wt%* of Ni(OH)$_2$ particles. The XRD pattern confirms that Ni was deposited by the suspension electrolysis of the insoluble Ni(OH)$_2$ particles. The surface of the deposit was composed of fine particles with diameters of approximately 30 nm. The cathodic

potential was approximately −0.70 V during electrolysis, and the current efficiency of reaction 5 was 0.1%, with electricity consumed for H$_2$ evolution (cathode limit: −0.28 V, Fig. 14). Steady-state polarization curves were obtained for the 50 *wt%* NaOH–H$_2$O electrolyte (Fig. 16), which revealed that the polarization was higher in the electrolyte comprising Fe$_2$O$_3$ and Ni(OH)$_2$ particles than that comprising only Fe$_2$O$_3$ particles, which corresponds to a simultaneous reduction of the Fe$_2$O$_3$ and Ni(OH)$_2$ particles.

To investigate the possible formation of Fe–Ni using our method, suspension electrolysis was conducted in 50 *wt%* of NaOH–H$_2$O + Fe$_2$O$_3$ (40 *wt%*)+Ni(OH)$_2$ (2.0 *wt%*) as the electrolyte at 383 K.
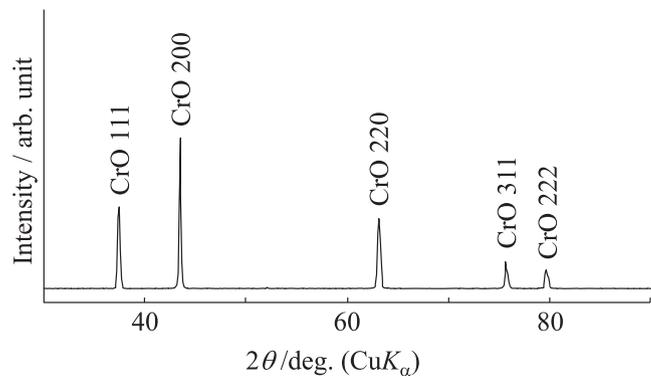
Figure 11. XRD patterns of the powder after electrolysis (0.1 A; 48 h) using Cr_2O_3 powder piled on a carbon-sheet cathode in 50 *wt%* of NaOH–H_2O at 383 K.

Figure 13. Current efficiency as a function of current density for the formation of Fe–Cr in 50 *wt%* of NaOH–H_2O + Fe_2O_3 (33 *wt%*) + Cr_2O_3 at 383 K. Quantity of electricity: 1080C.
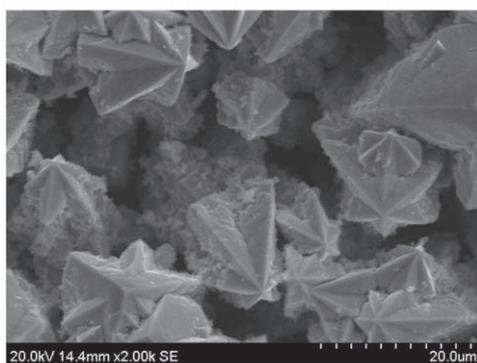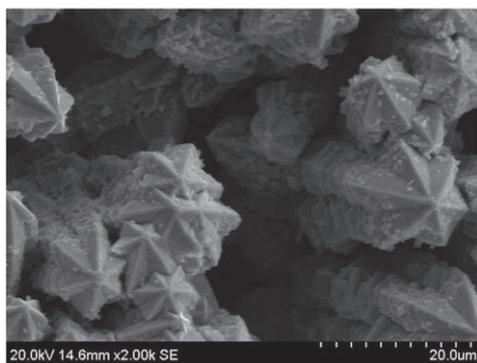
Figure 12. SEM images of Fe–Cr deposits obtained after electrolysis in 50 *wt%* of NaOH–H_2O + Fe_2O_3 (33 *wt%*) + Cr_2O_3 (10 *wt%*) at 383 K. Current density: 100 (a) and 200 (b) mA·cm^{-2} Quantity of electricity: 1080C.
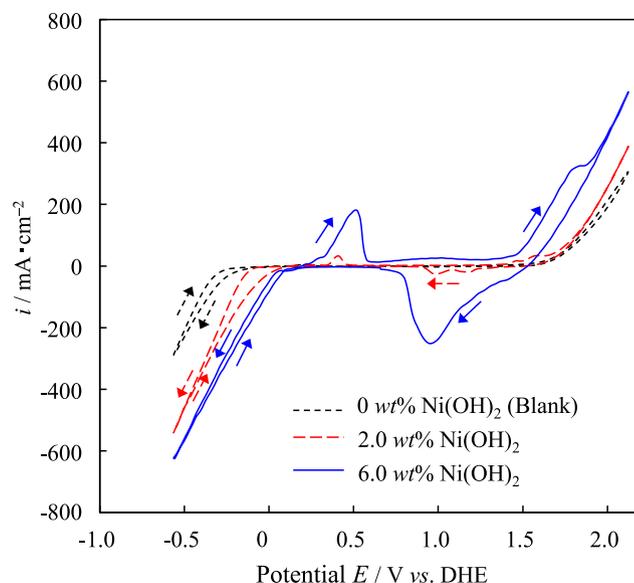
Figure 14. Typical cyclic voltammograms for a rotating graphite disk (1000 rpm) in 50 *wt%* of NaOH–H_2O + Ni(OH)$_2$ at 383 K. The scan rate was 10 mV·s^{-1}.

Table III. EDS-determined composition of the Fe–Ni deposit obtained on the cathode after electrolysis (100 mA·cm−2, 6 h) in 50 *wt*% of NaOH-H2O + Fe2O3 (40 *wt%*) +Ni(OH)2 (2.0 *wt%*) at 383 K.

Element	*wt%*	*at%*
Fe	96.0	96.2
Ni	4.00	3.80

Figure 17 shows a typical chronopotentiogram for the rotating-graphite-disk cathode during electrolysis (100 mA·cm^{-2}, 6 h). The cathode potential was approximately −0.05 V during electrolysis, which was more positive than the cathode limit, suggesting that Fe_2O_3 and Ni(OH)$_2$ were simultaneously reduced. The XRD pattern of the obtained deposit exhibited a peak pattern corresponding only to the *bcc* Fe–Ni solid solution (Fig. 18). EDS was used to evaluate the Fe–Ni composition of the obtained deposit (Table III): Ni was

found to coexist with Fe, and the formation of $Fe_{96}Ni_4$ was confirmed. The current efficiency for $Fe_{96}Ni_4$ formation via reactions 1, 2, and 5 was determined to be 40%. SEM images (Fig. 19)

a

b
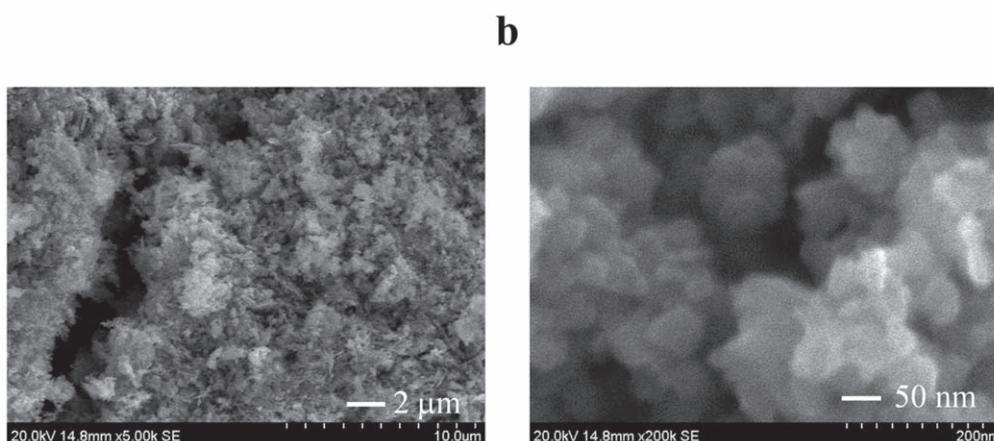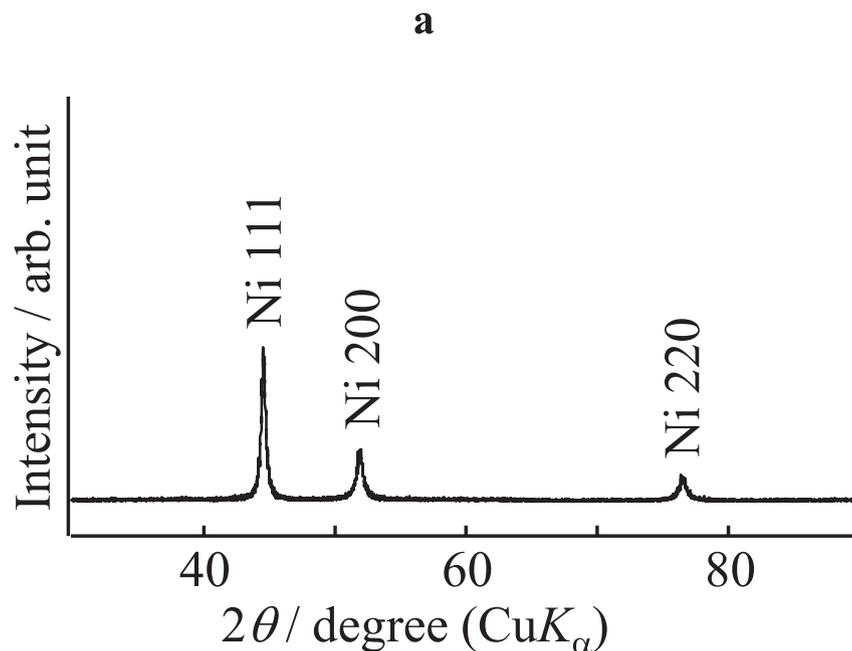
Figure 15. XRD pattern (a) and SEM images (b) of the deposit obtained after electrolysis (1.0 A·cm^{-2}, 12 h) in 50 *wt%* of NaOH–H$_2$O + Ni(OH)$_2$ (6.0 *wt%*) at 383 K.

revealed that the deposit comprised particles with diameters of approximately 1.0 μm, which were significantly larger than those of pure Ni (Fig. 15b) but identical to those of pure Fe[1] and Fe–Cr deposits. Therefore, the Fe crystal growth was inferred to predominate Ni deposition on Fe to form the Fe–Ni alloy.

The SEM images and EDS data for the Fe–Ni deposit obtained after the electrolysis (200 mA·cm^{-2}, 6 h) are shown in Fig. 20 and Table IV. The particle size of the deposit decreased with increasing current density. The Ni ratio of the obtained Fe–Ni deposit was higher at a higher current density and Ni(OH)$_2$ content, and the current efficiencies for Fe–Ni formation were approximately 50%. The Fe–Ni deposits were formed by suspension electrolysis at various current densities in 50 *wt%* NaOH–H$_2$O+Fe$_2$O$_3$ (20 *wt%*)+Ni(OH)$_2$ (20 *wt%*); the SEM images and EDS data for the Fe–Ni are shown in Figs. 21–22 and Table V, which confirmed that the Fe$_{71}$Ni$_{29}$ and Fe$_{68}$Ni$_{32}$ deposits were formed as disordered columns. These results confirmed that the Fe–Ni composition was controlled by the Ni(OH)$_2$ particle content and, to some extent, the current density. During electrolysis, the cathodic potential was unstable and the current efficiency for Fe–Ni formation was

Table IV. EDS-determined compositions of the Fe–Ni deposits obtained after electrolysis (200 mA·cm^{-2}) in 50 *wt%* of NaOH–H$_2$O + Fe$_2$O$_3$ (40 *wt%*)+Ni(OH)$_2$ at 383 K. Ni(OH)$_2$ content: (a) 2.0 *wt%* and (b) 4.0 *wt%* Quantity of electricity: 2160 C.

Element	*wt%*	*at%*
(a)		
Fe	93.3	93.6
Ni	6.70	6.40
(b)		
Fe	92.2	92.5
Ni	7.80	7.50

*Current efficiency: 46%.
 *Current efficiency: 48%.

approximately 10%, owing to the anomalous behavior of Fe–Ni codeposition and a high Ni(OH)$_2$ content (20 *wt%*). The Ni(OH)$_2$ particles were larger and less uniform than the Fe$_2$O$_3$ particles
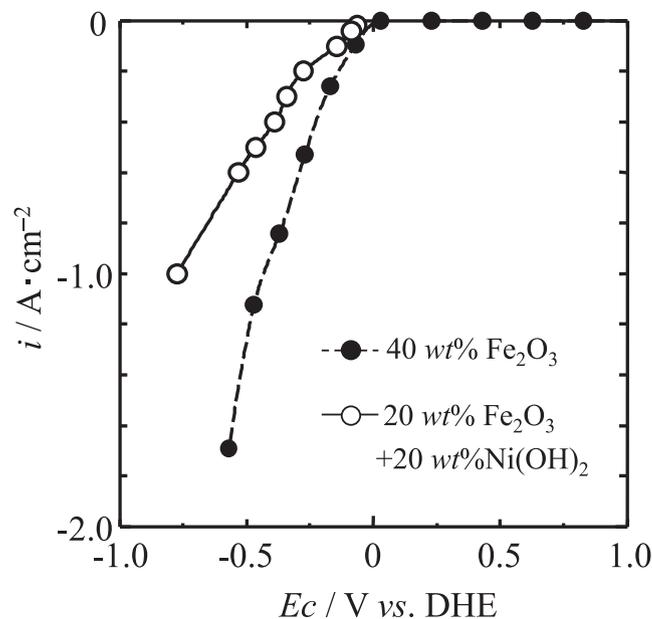
Figure 16. Typical steady-state polarization curves obtained in a 50 *wt%* NaOH–H$_2$O electrolyte at 383 K.
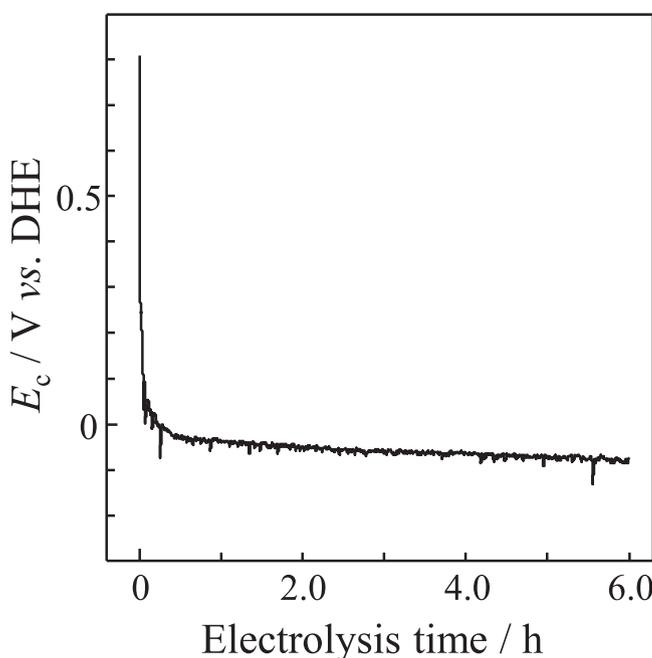
Figure 17. A typical chronopotentiogram for the rotating-graphite-disk cathode during electrolysis (100 mA·cm^{-2}, 6 h) in 50 *wt%* of NaOH–H$_2$O + Fe$_2$O$_3$ (40 *wt%*) + Ni(OH)$_2$ (2.0 *wt%*) at 383 K.

Figure 18. XRD pattern of the deposits obtained on the cathode after electrolysis (100 mA·cm^{-2}, 6 h) in 50 *wt%* of NaOH–H$_2$O + Fe$_2$O$_3$ (40 *wt%*) + Ni(OH)$_2$ (2.0 *wt%*) at 383 K.
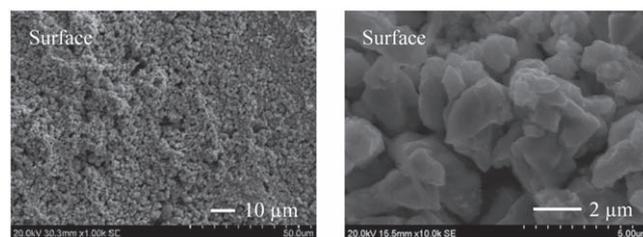
Figure 19. SEM images of the Fe–Ni deposits obtained on the cathode after electrolysis (100 mA·cm^{-2}, 6 h) in 50 *wt%* of NaOH–H$_2$O + Fe$_2$O$_3$ (40 *wt%*) + Ni(OH)$_2$ (2.0 *wt%*) at 383 K.

Table V. EDS-determined compositions of the Fe–Ni deposits obtained after electrolysis in 50 *wt%* of NaOH–H$_2$O + Fe$_2$O$_3$ (20 *wt%*)+Ni(OH)$_2$ (20 *wt%*) at 383 K. (a)200 mA·cm^{-2}, 6 h and (b) 400 mA·cm^{-2}, 3 h.

Element (a)	*wt%*	*at%*
Fe	70.0	71.0
Ni	30.0	29.0
(b)		
Fe	67.3	68.4
Ni	32.7	31.6

*Current efficiency: 9.7%.
  *Current efficiency: 9.0%.

(Figs. 5a and 5c). Large Ni(OH)$_2$ particles were not reduced immediately, and the unreacted Ni(OH)$_2$ was adsorbed on the cathode surface, inhibiting electrolysis. Therefore, smaller Ni(OH)$_2$ particles were used to decrease the amount of unreacted Ni(OH)$_2$ covering the cathode and improve the current efficiency. Particles approximately 1.0 μm in diameter formed 2.0-micrometer-wide and 30-micrometer-long columns. The column-forming particles decreased in size and spindled columns were formed at a higher current density. This trend has also been observed in the formation of Fe from hematite particles[1] and during Fe–Cr production in this study and may be attributed to the overpotential-dependence of the crystal-growth rate; crystals grow faster and are vertically spindled at a high overpotential.

Conclusions

We produced iron alloys by suspension electrolysis in a 50 *wt%* NaOH–H$_2$O electrolyte at 383 K. Fe–Cr and Fe–Ni alloys were produced using suspensions of Fe$_2$O$_3$+Cr$_2$O$_3$ and Fe$_2$O$_3$+Ni(OH)$_2$ particles, respectively. Highly ordered Fe–Cr columns were obtained on a disk cathode with a current efficiency that exceeded 90% at 100–300 mA·cm^{-2}; Cr$_2$O$_3$ was reduced by two steps, with CrO as an intermediate. Fe$_2$O$_3$ and Cr$_2$O$_3$ particles were directly reduced on
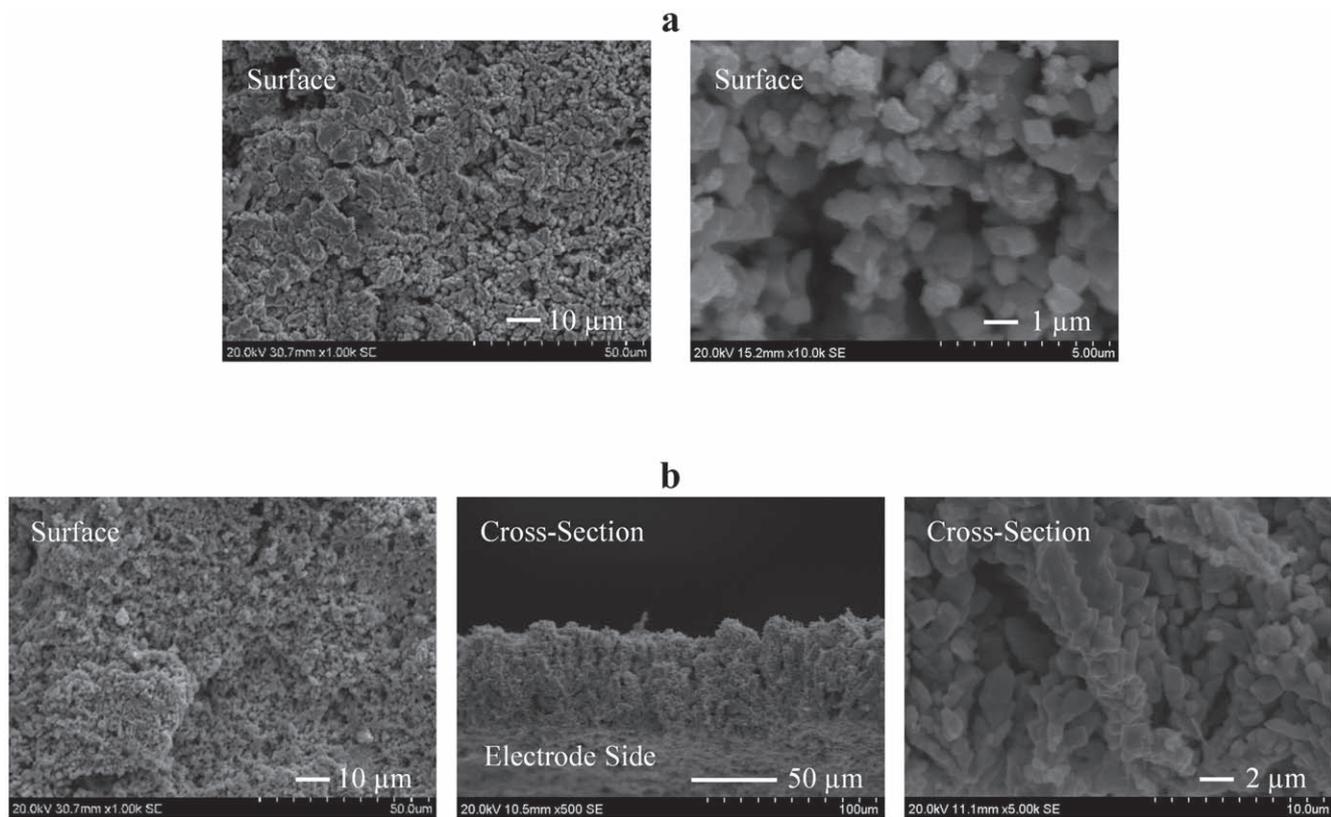
Figure 20. SEM images of the Fe–Ni deposits obtained on the cathode after electrolysis (200 mA$\cdot$cm^{-2}, 6 h) in 50 *wt%* of NaOH–H$_2$O + Fe$_2$O$_3$ (40 *wt%*) + Ni(OH)$_2$ at 383 K. Ni(OH)$_2$ content: 2.0 *wt%* (a) and 4.0 *wt%* (b).
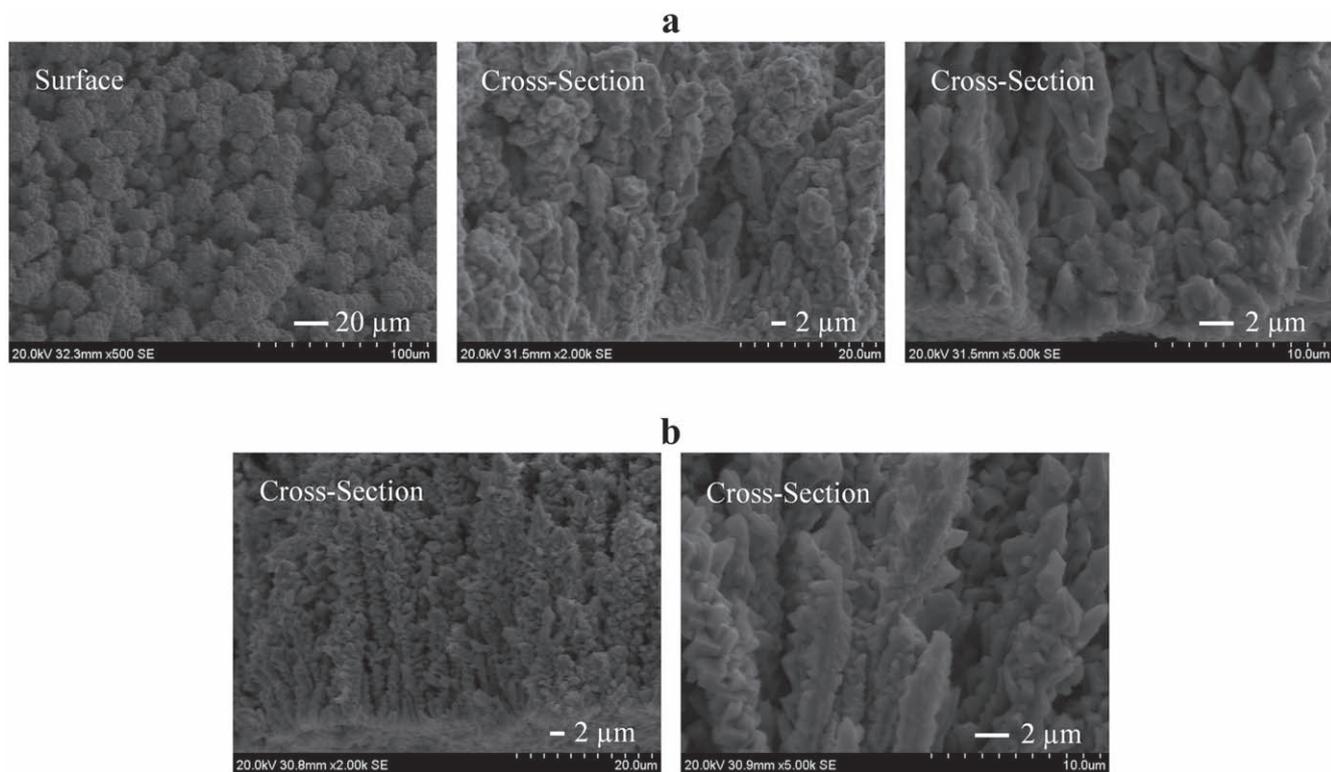
Figure 21. SEM images of the deposit obtained after electrolysis in 50 *wt%* of NaOH–H$_2$O + Fe$_2$O$_3$ (20 *wt%*) + Ni(OH)$_2$ (20 *wt%*) at 383 K. 200 mA$\cdot$cm^{-2} for 6 h (a) and 400 mA$\cdot$cm^{-2} for 3 h (b).
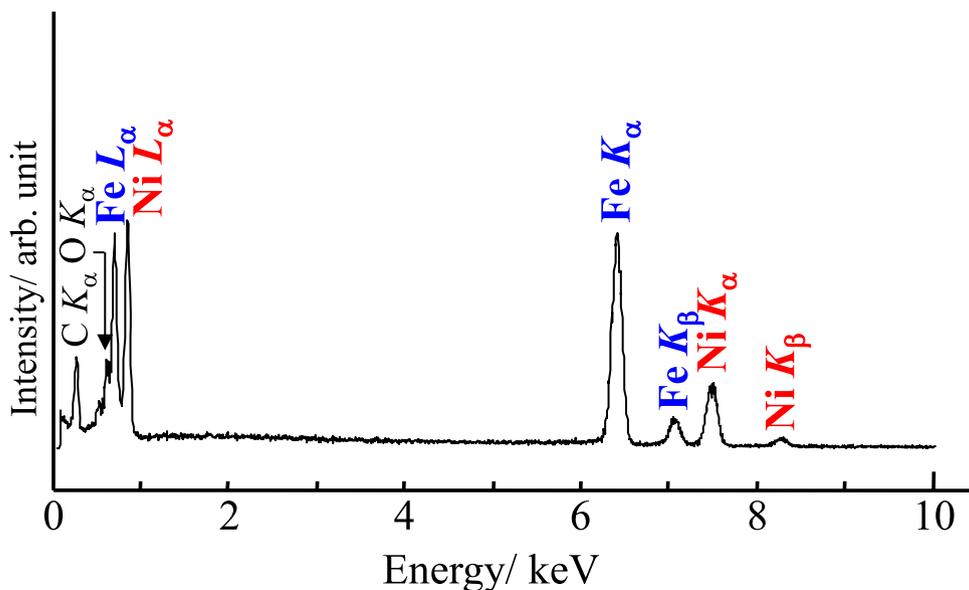
Figure 22. A typical EDS spectrum of the Fe–Ni deposit obtained after electrolysis (400 mA·cm^{-2}, 3 h) in 50 *wt*% of NaOH–H$_2$O + Fe$_2$O$_3$ (20 *wt*%) + Ni(OH)$_2$ (20 *wt*%) at 383 K.

the surface of the disk cathode to form columnar deposits consisting of cubic Fe–Cr particles with side lengths of approximately 5.0 μm. The columnar structure was strongly dependent on the current density and Fe$_2$O$_3$/Cr$_2$O$_3$ ratio. In contrast, Fe–Ni was deposited on the disk cathode using an electrolyte composed of Fe$_2$O$_3$ and Ni(OH)$_2$ particles, with a current efficiency of approximately 50% at 200 mA·cm^{-2}. Although the Fe–Ni particles grew in a columnar manner, they were disordered. Iron alloys with compositions in the stainless-steel region were produced using this method, and the alloy compositions were dependent on the Fe$_2$O$_3$/Cr$_2$O$_3$ or Fe$_2$O$_3$/Ni(OH)$_2$ content ratio.

ORCID

Manabu Tokushige ⓘ https://orcid.org/0000-0002-5724-233X

References

1. M. Tokushige, O. E. Kongstein, and G. M. Haarberg, *ECS Trans.*, **50**, 103 (2013).
2. B. Yuan, O. E. Kongstein, and G. M. Haarberg, *J. Electrochem. Soc.*, **156**, D64 (2009).
3. S. H. Tang and G. M. Haarberg, *ECS Trans.*, **28**, 309 (2010).
4. G. M. Haarberg and B. Yuan, *ECS Trans.*, **58**, 19 (2014).
5. A. Allanore, H. Lavelaine, G. Valentin, J. P. Birat, and F. Lapicque, *J. Electrochem. Soc.*, **154**, E187 (2007).
6. A. Allanore, H. Lavelaine, G. Valentin, J. P. Birat, and F. Lapicque, *J. Electrochem. Soc.*, **155**, E125 (2008).
7. A. Allanore, J. Feng, H. Lavelaine, and K. Ogle, *J. Electrochem. Soc.*, **157**, E24 (2010).
8. V. Feynerol, H. Lavelaine, P. Marlier, M. -N. Pons, and F. Lapicque, *J. Appl. Electrochem.*, **47**, 1339 (2017).
9. S. Gu, X. Zou, and X. Lu, *Appl. Mech. Mat.*, **595**, 8 (2014).
10. G. Picard, D. Oster, and B. Tremillon, *J. Chem. Res. (S)*, **8**, 252 (1980).
11. C. W. Bale et al., *Calphad*, **54**, 35 (2016).
12. G. Kaptay, *Electrochim. Acta*, **60**, 401 (2012).
13. M. E. Wagner and A. Allanore, *Electrochim. Acta*, **389**, 138442 (2021).
14. G. Fuseya and K. Sasaki, *Trans. Electrochem. Soc.*, **59**, 445 (1931).
15. F. Wang, K. Itoh, and T. Watanabe, *Mater. Trans.*, **43**, 439 (2002).
16. F. Wang and T. Watanabe, *Mat. Sci. Eng. A*, **349**, 183 (2003).
17. S. Yagi, K. Murase, T. Hirato, and Y. Awakura, *J. Electrochem. Soc.*, **154**, D304 (2007).
18. S. Yagi, K. Murase, T. Hirato, and Y. Awakura, *ECS Trans.*, **11**, 23 (2008).
19. C. Su, L. Zhao, L. Tian, B. Wen, M. Xiang, W. Bai, and J. Guo, *Coatings*, **9**, 56 (2019).
20. V. Torabinejad, M. Aliofkhazraei, S. Assareh, M. H. Allahyarzadeh, and A. S. Rouhaghdam, *J. Alloys Compd.*, **691**, 841 (2017).
21. I. Tabakovic, J. Gong, S. Riemer, and M. Kautzky, *J. Electrochem. Soc.*, **162**, D102 (2015).
22. A. S. Zadeh, K. Raeissi, and A. Saidi, *J. Alloy. Compd.*, **485**, 402 (2009).
23. H. Li and F. Ebrahimi, *Mater. Sci. Eng. A*, **347**, 93 (2003).
24. S. D. Leith, S. Ramli, and D. T. Schwartz, *J. Electrochem. Soc.*, **146**, 1431 (1999).
25. N. Zech, E. J. Podlaha, and D. Landolt, *J. Electrochem. Soc.*, **146**, 2886 (1999).
26. T. Krause, L. Arulnayagam, and M. Pritzker, *J. Electrochem. Soc.*, **144**, 960 (1997).
27. V. C. Kieling, *Surf. Coat. Tech.*, **96**, 135 (1997).
28. J. Horkans, *J. Electrochem. Soc.*, **128**, 45 (1981).
29. A. Brenner, *Electrodeposition of Alloys* (Academic Press, New York, NY) (1963).
30. H. Dahms, *J. Electroanal. Chem. Interfacial Electrochem.*, **8**, 5 (1964).
31. H. Dahms and I. M. Croll, *J. Electrochem. Soc.*, **112**, 771 (1965).
32. S. Hessami and C. W. Tobias, *J. Electrochem. Soc.*, **136**, 3611 (1989).
33. S. V. Mattigod, D. Rai, A. R. Felmy, and L. Rao, *J. Sol. Chem.*, **26**, 391 (1997).
34. M. W. Chase Jr, "JANAF thermochemical tables." *J. Phys. Chem. Ref. Data* (American Chemical Society and American Institute of Physics for the National Bureau of Standards, New York, NY) 4th ed. (1998).
35. V. Dufek, F. Petrů, and V. Brožek, *Monatsh. Chem.*, **98**, 2424 (1967).
36. M. Yasuda, F. Takeya, and F. Hine, *Corrosion*, **39**, 399 (1983).
37. P. C. Andricacos and L. T. Romankiw, *Advances in Electrochemical Science and Engineering* (VCH Publishers Inc, New York, NY) 3 (1990).